Available online at www.sciencedirect.com
ScienceDirect
Comput. Methods Appl. Mech. Engrg. 313 (2017) 239–258
Computer methods in applied mechanics and engineering
www.elsevier.com/locate/cma

A level-set based IGA formulation for topology optimization of flexoelectric materials

Hamid Ghasemi[c], Harold S. Park[d], Timon Rabczuk[a,b,c,*]

[a] *Division of Computational Mechanics, Ton Duc Thang University, Ho Chi Minh City, Viet Nam*
[b] *Faculty of Civil Engineering, Ton Duc Thang University, Ho Chi Minh City, Viet Nam*
[c] *Institute of Structural Mechanics, Bauhaus-Universität Weimar, Marienstraße 15, 99423 Weimar, Germany*
[d] *Dep. of Mechanical Eng, Boston University, Boston, MA 02215, USA*

Received 4 May 2016; received in revised form 22 September 2016; accepted 24 September 2016
Available online 2 October 2016

Highlights

- NURBS elements are successfully employed to model the flexoelectric effect in dielectrics.
- Topology optimization of flexoelectric micro and nanostructures can enhance their energy conversion efficiency.
- An efficient design methodology based on a combination of isogeometric analysis (IGA), level set and point wise density mapping techniques is presented.
- The point wise density mapping is directly used in the weak form of the governing equations and its derivative is consistently derived using adjoint sensitivity technique.

Abstract

This paper presents a design methodology based on a combination of isogeometric analysis (IGA), level set and point wise density mapping techniques for topology optimization of piezoelectric/flexoelectric materials. The fourth order partial differential equations (PDEs) of flexoelectricity, which require at least C^1 continuous approximations, are discretized using Non-Uniform Rational B-spline (NURBS). The point wise density mapping technique with consistent derivatives is directly used in the weak form of the governing equations. The boundary of the design domain is implicitly represented by a level set function. The accuracy of the IGA model is confirmed through numerical examples including a cantilever beam under a point load and a truncated pyramid under compression with different electrical boundary conditions. Finally, we provide numerical examples demonstrating the significant enhancement in electromechanical coupling coefficient that can be obtained using topology optimization.

Keywords: Flexoelectricity; Topology optimization; Level set; Isogeometric analysis (IGA); Micro-nanostructure

* Corresponding author.
E-mail addresses: hamid.ghasemi@uni-weimar.de (H. Ghasemi), parkhs@bu.edu (H.S. Park), timon.rabczuk@tdt.edu.vn (T. Rabczuk).

http://dx.doi.org/10.1016/j.cma.2016.09.029
0045-7825/

Nomenclature

$\boldsymbol{B}_u$, $\boldsymbol{B}_\theta$	The matrices containing the gradient of the $\boldsymbol{N}_u$ and $\boldsymbol{N}_\theta$
$\boldsymbol{C}/C_{ijkl}$	The fourth-order elasticity tensor
D_Ω	The whole structural domain
$\boldsymbol{d}/d_{ijkl}$	The fourth-order converse flexoelectric tensor
D_j^s	The surface gradient operator
D^n	The normal gradient operator
$\widehat{D}_i$	The usual electric displacements
$\widetilde{D}_{ij}$	The higher-order electric displacements
D_i	The physical electric displacements
$\boldsymbol{E}/E_i$	The electric field
$\boldsymbol{e}/e_{ikl}$	The third-order tensor of piezoelectricity
$\boldsymbol{f}/f_{ijkl}$	The fourth-order direct flexoelectric tensor
$\boldsymbol{G}_i/\boldsymbol{G}_{i,j}$	The control points in 1D/2D
H	The total electrical enthalpy
$\mathcal{H}$	The electric enthalpy density considering both piezoelectric and flexoelectric effects
$\overline{\mathcal{H}}$	The electric enthalpy density considering only piezoelectric effect
$\boldsymbol{H}_u$	The matrix containing the Hessian of the $\boldsymbol{N}_u$
$\widetilde{H}(\Phi)$	The smooth approximation of the Heaviside function
K_E	The kinetic energy for the system
k_{eff}^2	The electromechanical coupling coefficient
l	The Lagrangian objective function
mcp	The number of basis functions corresponding to $M_{j,q}(\eta)$
$M_{j,q}(\eta)$	The B-spline basis functions in Y direction
$\boldsymbol{n}/n_i$	The unit normal to the boundary $\partial\Omega$
$\boldsymbol{N}_u$	The basis functions corresponding to displacements
$\boldsymbol{N}_\theta$	The basis functions corresponding to electric potential
$N_{i,j}^{p,q}/N_{i,p}(\xi)$	The B-spline basis functions in X direction
ncp	The number of basis functions corresponding to $N_{i,p}(\xi)$
$\boldsymbol{P}/P_i$	The electric polarization
$\boldsymbol{p}/p_{ijk}$	The third order piezoelectric tensor
p	The polynomial order of basis functions corresponding to $N_{i,p}(\xi)$
q	The polynomial order of basis functions corresponding to $M_{j,q}(\eta)$
$R_i^p(\xi)/R_{i,j}^{p,q}(\xi,\eta)$	The NURBS basis functions
$\overline{r}_k$	The prescribed higher order traction
$\overline{t}_k$	The prescribed tractions
$\boldsymbol{u}$	The mechanical displacements
$\overline{u}_i$	The prescribed mechanical displacements
$\boldsymbol{V}$	The velocity vector
V_f/V_{f0}	The total/arbitrary volume
V_n	The normal component of the velocity vector
$\overline{v}_i$	The prescribed normal derivative of displacement
W_{ext}	The work done by the external surface mechanical and electrical forces
$W(\xi)$	The weighting function
w_i	The ith weight
w_{elec}	The electrical energy
w_{mech}	The mechanical (or strain) energy
Y	The Young's modulus
δ	The variation operator
$\tilde{\delta}(\Phi)$	The approximate Dirac delta function

$\boldsymbol{\varepsilon}/\varepsilon_{ij}$	The mechanical strain
η_i	The ith knot in Y direction
$\boldsymbol{\theta}$	The electric potential
$\overline{\theta}$	The prescribed electric potential
$\boldsymbol{\kappa}/\kappa_{ij}$	The second-order dielectric tensor
$\boldsymbol{\mu}/\mu_{ijkl}$	The fourth-order total flexoelectric tensor
ν	The Poisson's ratio
ξ_i	The ith knot in X direction
$\rho/\rho\,(\boldsymbol{x})$	The density function
ϱ	The density
$\hat{\sigma}_{ij}$	The usual stress
$\tilde{\sigma}_{ijk}$	The higher-order stress
σ_{ij}	The physical stress
Δ	The width of numerical approximation
$\boldsymbol{\varphi}/\varphi_{i,j}$	The corresponding nodal values of level set function
$\Phi(\boldsymbol{x})$	The level set function
ψ	The Lagrange multiplier
Ω	The admissible shape/domain
$\partial\Omega$	The boundary of Ω
ω	The surface charge density

1. Introduction

The piezoelectric effect, which only exists in materials with non-centrosymmetric crystal structures, refers to a linear dependence between the electric polarization, $\boldsymbol{P}$ and the mechanical strain, $\boldsymbol{\varepsilon}$ given by

$$P_i = p_{ijk}\varepsilon_{jk} \tag{1}$$

where $\boldsymbol{p}$ is the third order piezoelectric tensor [1–4]. In contrast to piezoelectricity, flexoelectricity is possible in all dielectrics, including those with centrosymmetric crystal structures, and is thus a more general electromechanical coupling mechanism. When flexoelectric effects are accounted for, the polarization is written as

$$P_i = p_{ijk}\varepsilon_{jk} + \mu_{ijkl}\frac{\partial \varepsilon_{jk}}{\partial x_l} \tag{2}$$

where the electric polarization exhibits a linear response to the gradient of mechanical strain [5]. In Eq. (2) μ_{ijkl} are the flexoelectric coefficients; the first term on the right hand side is zero for non-piezoelectric materials.

Flexoelectricity in solids was introduced by Mashkevich and Tolpygo [6] in the 1950s but received little attention, likely because the flexoelectric effect is relatively insignificant for bulk crystalline materials. However recent developments in nanotechnology have shed a new light on flexoelectricity as a size dependent phenomenon due to the large strain gradients that are obtainable at small length scales, or alternatively in soft materials like biological membranes [7]. For additional recent reviews on flexoelectricity we refer interested readers to [8,9].

While the theoretical basis for flexoelectricity in dielectrics has been developed in detail [1,10,11], there have been a correspondingly small number of numerical studies. Recently, Abdollahi et al. presented a computational framework to evaluate the flexoelectric effect in dielectric solids using a meshfree method in 2D [12] and 3D [13]. They showed that available simplified analytical solutions only provide order of magnitude estimates in comparison with a more general model which considers the multidimensional coupling effects.

Topology optimization is a powerful approach that optimizes the material distribution within the design domain. The first computational model for topology optimization was presented by Bendsøe and Kikuchi [14]. Topology optimization has since been successfully applied to a variety of applications such as structural design [15], compliant mechanism [16] and microelectromechanical system [17,18]. To the best of our knowledge, employing topology optimization for dielectric solids in order to enhance their flexoelectric behavior has not been done to-date.

Various techniques have been developed for topology optimization. Among them, the Solid Isotropic Material with Penalization (SIMP) technique [19] is very common due to its simplicity. Although this technique has been widely applied to different problems, researchers have encountered difficulties with its numerical stability in some multiphysics and multiconstraint problems [20]. Furthermore, in multiphysics problems the different sets of penalization parameters will directly and noticeably impact the final results in terms of the stability of the solution and the distinct void-solid representation.

To overcome the above mentioned difficulties, we use the Level Set Method (LSM) [21] for topology optimization in order to exploit its intrinsic flexibility in handling topological changes. In the LSM, the boundaries of the domain are implicitly represented with a scalar level set function which changes in time, providing unique benefits such as smooth boundaries and distinct interfaces, integrated shape and topology optimization. We also use IGA instead of standard finite elements method (FEM) because the fourth order PDEs of flexoelectricity demand at least C^1 continuous basis functions in a Galerkin method [12]. IGA also enables using the same data set for the analysis and the optimization as well as an exact representation of the geometry.

The remainder of this paper is organized as follows: in Section 2 we introduce the theory of flexoelectricity; the discretization based on IGA is presented in Section 3; Section 4 contains the topology optimization based on the LSM; afterwards, numerical examples in Section 5 and concluding remarks in Section 6 are presented.

2. Flexoelectricity: theory and formulation

For a linear dielectric solid possessing only the piezoelectric effect, the electric enthalpy density, $\overline{\mathcal{H}}$, is a function of $\boldsymbol{\varepsilon}$ and $\boldsymbol{E}$, i.e. $\overline{\mathcal{H}}(\varepsilon_{ij}, E_i)$. When flexoelectric effects are accounted for, the enthalpy density, $\mathcal{H}$, also becomes a function of the strain gradient and electric field gradient. Thus

$$\mathcal{H}\left(\varepsilon_{ij}, E_i, \varepsilon_{jk,l}, E_{i,j}\right) = \frac{1}{2}C_{ijkl}\varepsilon_{ij}\varepsilon_{kl} - e_{ikl}E_i\varepsilon_{kl} + \left(d_{ijkl}E_{i,j}\varepsilon_{kl} + f_{ijkl}E_i\varepsilon_{jk,l}\right) - \frac{1}{2}\kappa_{ij}E_iE_j \tag{3a}$$

where $E_i = -\theta_{,i}$ is the electric field; $\boldsymbol{\theta}$ is the electric potential; $\boldsymbol{\varepsilon}$ is the mechanical strain; $\boldsymbol{e}$ is the third-order tensor of piezoelectricity; $\boldsymbol{\kappa}$ is the second-order dielectric tensor; $\boldsymbol{C}$ is the fourth-order elasticity tensor; $\boldsymbol{f}$ is the fourth-order direct flexoelectric tensor and $\boldsymbol{d}$ is the fourth-order converse flexoelectric tensor [12]. Let us consider the terms in the brackets on the RHS of Eq. (3a) containing the direct and reverse flexoelectric effects. Integrating these terms over the volume and using integration by parts and the Gauss divergence theorem on the first term yields

$$\begin{aligned}
\int_\Omega \left(d_{ijkl}E_{i,j}\varepsilon_{kl} + f_{ijkl}E_i\varepsilon_{jk,l}\right)d\Omega &= \int_\Omega d_{ijkl}E_{i,j}\varepsilon_{kl}d\Omega + \int_\Omega f_{ijkl}E_i\varepsilon_{jk,l}d\Omega \\
&= \int_{\partial\Omega} d_{ijkl}E_i\varepsilon_{kl}ds - \int_\Omega d_{ijkl}E_i\varepsilon_{kl,j}d\Omega + \int_\Omega f_{ijkl}E_i\varepsilon_{jk,l}d\Omega \\
&= \int_\Omega \left(f_{ijkl}E_i\varepsilon_{jk,l} - d_{ijkl}E_i\varepsilon_{kl,j}\right)d\Omega + \int_{\partial\Omega} d_{ijkl}E_i\varepsilon_{kl}ds \\
&= -\int_\Omega \left(d_{iljk} - f_{ijkl}\right)E_i\varepsilon_{jk,l}d\Omega + \int_{\partial\Omega} d_{ijkl}E_i\varepsilon_{kl}ds \\
&= -\int_\Omega \mu_{ijkl}E_i\varepsilon_{jk,l}d\Omega + \int_{\partial\Omega} d_{ijkl}E_i\varepsilon_{kl}ds
\end{aligned} \tag{3b}$$

which is expressed in terms of only one material tensor, $\boldsymbol{\mu}$ where $\mu_{ijkl} = d_{iljk} - f_{ijkl}$. Therefore, we can rewrite Eq. (3a) as

$$\mathcal{H}\left(\varepsilon_{ij}, E_i, \varepsilon_{jk,l}\right) = \frac{1}{2}C_{ijkl}\varepsilon_{ij}\varepsilon_{kl} - e_{ikl}E_i\varepsilon_{kl} - \mu_{ijkl}E_i\varepsilon_{jk,l} - \frac{1}{2}\kappa_{ij}E_iE_j. \tag{4}$$

For a pure piezoelectric material we have

$$\sigma_{ij} = \frac{\partial\,\overline{\mathcal{H}}}{\partial\varepsilon_{ij}} \quad \text{and} \quad D_i = -\frac{\partial\,\overline{\mathcal{H}}}{\partial E_i} \tag{5}$$

while in the presence of flexoelectricity, the electromechanical stresses including the usual ($\hat{\sigma}_{ij}/\widehat{D}_i$), higher-order ($\tilde{\sigma}_{ijk}/\widetilde{D}_{ij}$) and physical ($\sigma_{ij}/D_i$) ones are defined through the following relations:

$$\hat{\sigma}_{ij} = \frac{\partial \mathcal{H}}{\partial \varepsilon_{ij}} \quad \text{and} \quad \widehat{D}_i = -\frac{\partial \mathcal{H}}{\partial E_i} \tag{6}$$

$$\tilde{\sigma}_{ijk} = \frac{\partial \mathcal{H}}{\partial \varepsilon_{ij,k}} \quad \text{and} \quad \widetilde{D}_{ij} = -\frac{\partial \mathcal{H}}{\partial E_{i,j}} \tag{7}$$

$$\sigma_{ij} = \hat{\sigma}_{ij} - \tilde{\sigma}_{ijk,k} \quad \text{and} \quad D_i = \widehat{D}_i - \widetilde{D}_{ij,j} \tag{8}$$

thus

$$\sigma_{ij} = \hat{\sigma}_{ij} - \tilde{\sigma}_{ijk,k} = C_{ijkl}\varepsilon_{kl} - e_{kij}E_k + \mu_{lijk}E_{l,k} \tag{9}$$

$$D_i = \widehat{D}_i - \widetilde{D}_{ij,j} = e_{ikl}\varepsilon_{kl} + \kappa_{ij}E_j + \mu_{ijkl}\varepsilon_{jk,l} \tag{10}$$

since $\widetilde{D}_{ij}$ has no contribution in Eq. (4) thus, the essential and natural electrical boundary conditions are the same as electrostatics. So,

$$\theta = \overline{\theta} \quad \text{on } \Gamma_\theta \tag{11}$$

$$D_i n_i = -\omega \quad \text{on } \Gamma_D \tag{12}$$

$$\Gamma_\theta \cup \Gamma_D = \partial\Omega \quad \text{and} \quad \Gamma_\theta \cap \Gamma_D = \emptyset \tag{13}$$

where $\overline{\theta}$ and ω are the prescribed electric potential and surface charge density; n_i is the unit normal to the boundary $\partial\Omega$ of the domain Ω. For the mechanical boundary conditions we have

$$u_i = \overline{u}_i \quad \text{on } \Gamma_u \tag{14}$$

$$t_k = n_j(\hat{\sigma}_{jk} - \tilde{\sigma}_{ijk,i}) - D_j^s(n_i\tilde{\sigma}_{ijk}) - (D_p^s n_p)n_i n_j \tilde{\sigma}_{ijk} = \overline{t}_k \quad \text{on } \Gamma_t \tag{15}$$

$$\Gamma_u \cup \Gamma_t = \partial\Omega \quad \text{and} \quad \Gamma_u \cap \Gamma_t = \emptyset \tag{16}$$

where $\overline{u}_i$ and $\overline{t}_k$ are the prescribed mechanical displacements and tractions; $D_j^s = \partial_j - n_j D^n$ is the surface gradient operator and $D^n = n_k\partial_k$ is the normal gradient operator. In addition to these, the strain gradients result in other types of boundary conditions as follows

$$u_{i,j}n_j = \overline{v}_i \quad \text{on } \Gamma_v \tag{17}$$

$$n_i n_j \tilde{\sigma}_{ijk} = \overline{r}_k \quad \text{on } \Gamma_r \tag{18}$$

$$\Gamma_v \cup \Gamma_r = \partial\Omega \quad \text{and} \quad \Gamma_v \cap \Gamma_r = \emptyset \tag{19}$$

where $\overline{v}_i$ and $\overline{r}_k$ are the prescribed normal derivative of displacement and the higher order traction, respectively.

We can rewrite Eqs. (6) and (7) as

$$\partial\mathcal{H} = \hat{\sigma}_{ij}\,\partial\varepsilon_{ij} \tag{20}$$

$$\partial\mathcal{H} = \tilde{\sigma}_{ijk}\,\partial\varepsilon_{ij,k} \tag{21}$$

$$\partial\mathcal{H} = -\widehat{D}_i\partial E_i \tag{22}$$

and then by integrating over Ω we obtain

$$H = \frac{1}{2}\int_\Omega \left(\hat{\sigma}_{ij}\varepsilon_{ij} + \tilde{\sigma}_{ijk}\varepsilon_{ij,k} - \widehat{D}_i E_i\right) d\Omega \tag{23}$$

where H is the total electrical enthalpy.

The work done by the external surface mechanical and electrical forces can be written as

$$W_{ext} = \int_{\Gamma_t} \overline{t}_i u_i dS - \int_{\Gamma_D} \omega\theta dS. \tag{24}$$

The kinetic energy for the system is also defined as

$$K_E = \frac{1}{2}\int_\Omega \varrho \dot{u}_i \dot{u}_i d\Omega \tag{25}$$

where ϱ denotes the density and the superimposed dot indicate time derivative.

Using Hamilton principle without the damping term we have

$$\delta \int_{t_1}^{t_2} (K_E - H + W_{ext})\, dt = 0 \tag{26a}$$

and

$$\delta \int_{t_1}^{t_2} \left(\frac{1}{2}\int_\Omega \varrho \dot{u}_i \dot{u}_i d\Omega - \frac{1}{2}\int_\Omega \left(\hat{\sigma}_{ij}\varepsilon_{ij} + \tilde{\sigma}_{ijk}\varepsilon_{ij,k} - \widehat{D}_i E_i\right) d\Omega + \int_{\Gamma_t} \bar{t}_i u_i dS - \int_{\Gamma_D} \omega\theta dS \right) dt = 0 \tag{26b}$$

moving the variation operation into the integral operations we obtain

$$\begin{aligned} &\int_{t_1}^{t_2} \left(\frac{1}{2}\int_\Omega \delta(\varrho \dot{u}_i \dot{u}_i) d\Omega - \frac{1}{2}\int_\Omega \delta\left(\hat{\sigma}_{ij}\varepsilon_{ij} + \tilde{\sigma}_{ijk}\varepsilon_{ij,k} - \widehat{D}_i E_i\right) d\Omega + \int_{\Gamma_t} \bar{t}_i \delta u_i dS \right. \\ &\quad \left. - \int_{\Gamma_D} \omega\delta\theta dS \right) dt \\ &= 0 \end{aligned} \tag{26c}$$

by changing the order of operations and using the chain rule of variation we have

$$\int_{t_1}^{t_2} \left[\frac{1}{2}\int_\Omega \delta(\varrho \dot{u}_i \dot{u}_i) d\Omega \right] dt = -\int_{t_1}^{t_2} \left[\int_\Omega \varrho\, (\delta u_i \ddot{u}_i)\, d\Omega \right] dt \tag{27}$$

$$\int_{t_1}^{t_2} \left[\frac{1}{2}\int_\Omega \delta\left(\hat{\sigma}_{ij}\varepsilon_{ij} + \tilde{\sigma}_{ijk}\varepsilon_{ij,k} - \widehat{D}_i E_i\right) d\Omega \right] dt = \int_{t_1}^{t_2} \left[\int_\Omega (\hat{\sigma}_{ij}\delta\varepsilon_{ij} + \tilde{\sigma}_{ijk}\delta\varepsilon_{ij,k} - \widehat{D}_i \delta E_i) d\Omega \right] dt. \tag{28}$$

Eq. (26c) now becomes

$$\begin{aligned} &\int_{t_1}^{t_2} \left(-\int_\Omega \varrho\, (\delta u_i \ddot{u}_i)\, d\Omega - \int_\Omega \left(\hat{\sigma}_{ij}\delta\varepsilon_{ij} + \tilde{\sigma}_{ijk}\delta\varepsilon_{ij,k} - \widehat{D}_i \delta E_i\right) d\Omega + \int_{\Gamma_t} \bar{t}_i \delta u_i dS \right. \\ &\quad \left. - \int_{\Gamma_D} \omega\delta\theta dS \right) dt = 0. \end{aligned} \tag{29}$$

To satisfy Eq. (29) for all possible choices of $\boldsymbol{u}$, the integrand of the time integration has to vanish, which leads to

$$\int_\Omega \varrho\, (\delta u_i \ddot{u}_i)\, d\Omega + \int_\Omega \left(\hat{\sigma}_{ij}\delta\varepsilon_{ij} + \tilde{\sigma}_{ijk}\delta\varepsilon_{ij,k} - \widehat{D}_i \delta E_i\right) d\Omega - \int_{\Gamma_t} \bar{t}_i \delta u_i dS + \int_{\Gamma_D} \omega\delta\theta dS = 0. \tag{30}$$

The inertia term is neglected for a static problem yielding

$$\int_\Omega \left(\hat{\sigma}_{ij}\delta\varepsilon_{ij} + \tilde{\sigma}_{ijk}\delta\varepsilon_{ij,k} - \widehat{D}_i \delta E_i\right) d\Omega - \int_{\Gamma_t} \bar{t}_i \delta u_i dS + \int_{\Gamma_D} \omega\delta\theta dS = 0. \tag{31a}$$

Substituting Eqs. (6)–(10) into Eq. (31a) yields

$$\begin{aligned} &\int_\Omega \left(C_{ijkl}\delta\varepsilon_{ij}\varepsilon_{kl} - e_{kij}E_k\delta\varepsilon_{ij} - \mu_{lijk}E_l\delta\varepsilon_{ij,k} - \kappa_{ij}\delta E_i E_j - e_{ikl}\delta E_i\varepsilon_{kl} - \mu_{ijkl}\delta E_i\varepsilon_{jk,l}\right) d\Omega \\ &\quad - \int_{\Gamma_t} \bar{t}_i \delta u_i dS + \int_{\Gamma_D} \omega\delta\theta dS = 0. \end{aligned} \tag{31b}$$

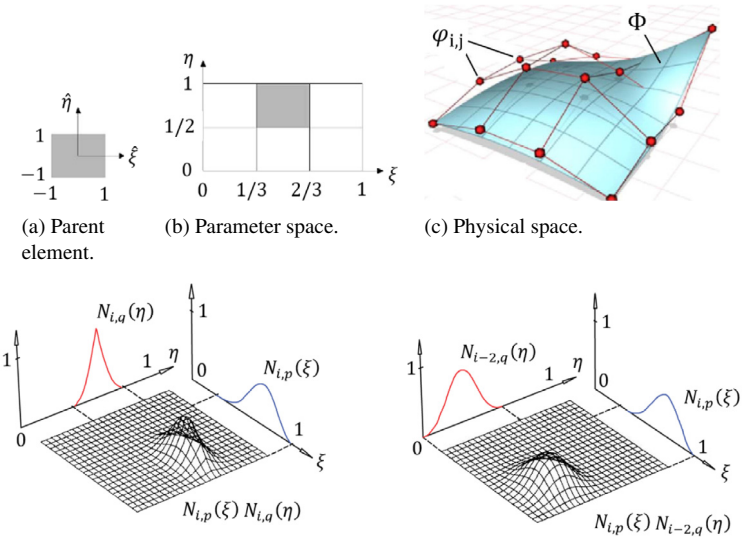

(a) Parent element. (b) Parameter space. (c) Physical space.

(d) Typical shape functions of order p and q.

Fig. 1. IGA concept: parent element (a), parameter space (b), physical space (c) and typical basis functions (d). The red dots represent control points.

3. Discretization

The key idea of IGA has been to unify CAD and CAE. However, our main motivation to use NURBS basis functions is their higher continuity (up to $p-1$, where p is polynomial order). It means that NURBS basis functions are up to $p-1$ times continuously differentiable across element boundaries.

There are two different spaces in IGA namely the physical space (Fig. 1(c)) and parameter space (Fig. 1(b)). Each element in the physical space is the image of a corresponding element in the parameter space. The parameter space is discretized by knot vectors. A knot vector in one dimension is a non-decreasing set of coordinates in the parameter space, written $\boldsymbol{\xi} = \{\xi_1, \xi_2, \ldots, \xi_{n+p+1}\}$, where $\xi_i \in \mathbb{R}$ is the ith knot, i is the knot index, $i = 1,\ 2, \ldots, ncp + p + 1$, p is the polynomial order and ncp is the number of basis functions.

Control points in IGA are used to discretize the geometry and define the degrees of freedom. As schematically shown in Fig. 1(c), they do not necessarily lie on the surface itself, but define its envelope. For approximation of the corresponding fields the values on control point are multiplied with their corresponding basis functions as shown in Fig. 1(d). The parent element (Fig. 1(a)) is used for numerical integration.

NURBS basis functions and derivatives

The NURBS basis is given by

$$R_i^p(\xi) = \frac{N_{i,p}(\xi)\, w_i}{W(\xi)} = \frac{N_{i,p}(\xi)\, w_i}{\sum_{i'=1}^{ncp} N_{i',p}(\xi)\, w_{i'}} \tag{32a}$$

where $N_{i,p}(\xi)$ are B-spline basis functions recursively defined by using Cox–de Boor formula and starting with piecewise constants ($p = 0$) [22]

$$N_{i,0}(\xi) = \begin{cases} 1 & \text{if } \xi_i \le \xi < \xi_{i+1} \\ 0 & \text{otherwise} \end{cases} \tag{32b}$$

and for $p = 1, 2, 3, \ldots$

$$N_{i,p}(\xi) = \frac{\xi - \xi_i}{\xi_{i+p} - \xi_i} N_{i,p-1}(\xi) + \frac{\xi_{i+p+1} - \xi}{\xi_{i+p+1} - \xi_{i+1}} N_{i+1,p-1}(\xi) \tag{32c}$$

w_i is referred to as the ith weight while $W(\xi)$ is the weighting function defined as follows:

$$W(\xi) = \sum_{i=1}^{ncp} N_{i,p}(\xi)\, w_i \tag{32d}$$

simply applying the quotient rule to Eq. (32a) yields:

$$\frac{d}{d\xi} R_i^p(\xi) = w_i \frac{W(\xi)\, N'_{i,p}(\xi) - W'(\xi)\, N_{i,p}(\xi)}{(W(\xi))^2} \tag{33a}$$

where,

$$N'_{i,p}(\xi) = \frac{p}{\xi_{i+p} - \xi_i} N_{i,p-1}(\xi) - \frac{p}{\xi_{i+p+1} - \xi_{i+1}} N_{i+1,p-1}(\xi) \tag{33b}$$

and

$$W'(\xi) = \sum_{i=1}^{ncp} N'_{i,p}(\xi)\, w_i. \tag{33c}$$

Among NURBS basis functions characteristics, the most important ones are partition of unity property, compact support of each basis functions and non-negative values. It can be also noted that if the weights are all equal, then $R_i^p(\xi) = N_{i,p}(\xi)$; so, B-spline is the special case of NURBS. Details related to higher order derivatives formulations can be found in [23].

NURBS curves and surfaces

A NURBS curve is defined as:

$$\boldsymbol{Crv}(\xi) = \sum_{i=1}^{ncp} R_i^p(\xi)\, \boldsymbol{G}_i \tag{34a}$$

where $\boldsymbol{G}_i \in \mathbb{R}^d$ are control points and $i = 1, 2, \ldots, ncp$, are the number of control points. Similarly, for definition of a NURBS surface, two knot vectors $\boldsymbol{\xi} = \{\xi_1, \xi_2, \ldots, \xi_{n+p+1}\}$ and $\boldsymbol{\eta} = \{\eta_1, \eta_2, \ldots, \eta_{m+q+1}\}$ (one for each direction) as well as a control net $\boldsymbol{G}_{i,j}$ are required. A NURBS surface is then defined as:

$$\boldsymbol{Srf}(\xi, \eta) = \sum_{i=1}^{ncp} \sum_{j=1}^{mcp} R_{i,j}^{p,q}(\xi, \eta)\, \boldsymbol{G}_{i,j} \tag{34b}$$

where $R_{i,j}^{p,q}(\xi, \eta)$ is defined according to the following equation, while $N_{i,p}(\xi)$ and $M_{j,q}(\eta)$ are univariate B-spline basis functions of order p and q corresponding to knot vector $\boldsymbol{\xi}$ and $\boldsymbol{\eta}$, respectively.

$$R_{i,j}^{p,q}(\xi, \eta) = \frac{N_{i,p}(\xi)\, M_{j,q}(\eta)\, w_{i,j}}{\sum_{i'=1}^{ncp} \sum_{j'=1}^{mcp} N_{i',p}(\xi)\, M_{j',q}(\eta) w_{i',j'}}. \tag{35}$$

In this work the NURBS basis functions are employed to approximate displacement $\boldsymbol{u}$ and electric potential $\boldsymbol{\theta}$ fields as well as their derivatives according to

$$u_h(x, y) = \sum_{i=1}^{ncp} \sum_{j=1}^{mcp} N_{i,j}^{p,q}(\xi, \eta)\, u_{ij}^e = (\boldsymbol{N}_u)^{\mathrm{T}} \boldsymbol{u}^e \tag{36a}$$

$$\theta_h(x, y) = \sum_{i=1}^{ncp} \sum_{j=1}^{mcp} N_{i,j}^{p,q}(\xi, \eta)\, \theta_{ij}^e = (\boldsymbol{N}_\theta)^{\mathrm{T}} \boldsymbol{\theta}^e \tag{36b}$$

$$\partial_j u_h = \partial_j \boldsymbol{N}_u \boldsymbol{u}^e = (\boldsymbol{B}_u)^{\mathrm{T}} \boldsymbol{u}^e = \boldsymbol{\varepsilon} \tag{36c}$$

$$\partial_j \theta_h = \partial_j \boldsymbol{N}_\theta \boldsymbol{\theta}^e = (\boldsymbol{B}_\theta)^{\mathrm{T}} \boldsymbol{\theta}^e = -\boldsymbol{E} \tag{36d}$$

$$\partial_j \partial_k u_h = \partial_j \partial_k \boldsymbol{N}_u \boldsymbol{u}^e = (\boldsymbol{H}_u)^{\mathrm{T}} \boldsymbol{u}^e \tag{36e}$$

where the superscript e denotes nodal parameters at the control points; $\boldsymbol{B}_u$, $\boldsymbol{B}_\theta$ and $\boldsymbol{H}_u$ are the matrices containing the gradient and Hessian of the corresponding basis functions (i.e. $\boldsymbol{N}_u$ and $\boldsymbol{N}_\theta$) which are defined as

$$\boldsymbol{B}_u = \begin{bmatrix} \frac{\partial N_1}{\partial x} & 0 & \frac{\partial N_1}{\partial y} \\ \frac{\partial N_2}{\partial x} & 0 & \frac{\partial N_2}{\partial y} \\ \vdots & \vdots & \vdots \\ \frac{\partial N_{ncp}}{\partial x} & 0 & \frac{\partial N_{ncp}}{\partial y} \\ 0 & \frac{\partial N_1}{\partial y} & \frac{\partial N_1}{\partial x} \\ 0 & \frac{\partial N_2}{\partial y} & \frac{\partial N_2}{\partial x} \\ \vdots & \vdots & \vdots \\ 0 & \frac{\partial N_{ncp}}{\partial y} & \frac{\partial N_{ncp}}{\partial x} \end{bmatrix}, \qquad \boldsymbol{B}_\theta = \begin{bmatrix} \frac{\partial N_1}{\partial x} & \frac{\partial N_1}{\partial y} \\ \vdots & \vdots \\ \frac{\partial N_{ncp}}{\partial x} & \frac{\partial N_{ncp}}{\partial y} \end{bmatrix},$$

$$\boldsymbol{H}_u = \begin{bmatrix} \frac{\partial^2 N_1}{\partial x^2} & 0 & \frac{\partial^2 N_1}{\partial y \partial x} & \frac{\partial^2 N_1}{\partial x \partial y} & 0 & \frac{\partial^2 N_1}{\partial y^2} \\ \frac{\partial^2 N_2}{\partial x^2} & 0 & \frac{\partial^2 N_2}{\partial y \partial x} & \frac{\partial^2 N_2}{\partial x \partial y} & 0 & \frac{\partial^2 N_2}{\partial y^2} \\ \vdots & \vdots & \vdots & \vdots & \vdots & \vdots \\ \frac{\partial^2 N_{ncp}}{\partial x^2} & 0 & \frac{\partial^2 N_{ncp}}{\partial y \partial x} & \frac{\partial^2 N_{ncp}}{\partial x \partial y} & 0 & \frac{\partial^2 N_{ncp}}{\partial y^2} \\ 0 & \frac{\partial^2 N_1}{\partial y \partial x} & \frac{\partial^2 N_1}{\partial x^2} & 0 & \frac{\partial^2 N_1}{\partial y^2} & \frac{\partial^2 N_1}{\partial x \partial y} \\ 0 & \frac{\partial^2 N_2}{\partial y \partial x} & \frac{\partial^2 N_2}{\partial x^2} & 0 & \frac{\partial^2 N_2}{\partial y^2} & \frac{\partial^2 N_2}{\partial x \partial y} \\ \vdots & \vdots & \vdots & \vdots & \vdots & \vdots \\ 0 & \frac{\partial^2 N_{ncp}}{\partial y \partial x} & \frac{\partial^2 N_{ncp}}{\partial x^2} & 0 & \frac{\partial^2 N_{ncp}}{\partial y^2} & \frac{\partial^2 N_{ncp}}{\partial x \partial y} \end{bmatrix}. \tag{37}$$

By substituting Eqs. (36a)–(36e) into Eq. (31b) we obtain after some algebra the following discrete system of equations

$$\begin{bmatrix} \boldsymbol{A}_{UU} & \boldsymbol{A}_{U\theta} \\ \boldsymbol{A}_{\theta U} & \boldsymbol{A}_{\theta\theta} \end{bmatrix} \begin{bmatrix} \boldsymbol{U} \\ \theta \end{bmatrix} = \begin{bmatrix} \boldsymbol{f}_U \\ \boldsymbol{f}_\theta \end{bmatrix} \tag{38}$$

where

$$\boldsymbol{A}_{UU} = \sum_e \int_{\Omega_e} (\boldsymbol{B}_u) \boldsymbol{C} (\boldsymbol{B}_u)^{\mathrm{T}} d\Omega_e \tag{39a}$$

$$\boldsymbol{A}_{U\theta} = \sum_e \int_{\Omega_e} [(\boldsymbol{B}_u) \boldsymbol{e} (\boldsymbol{B}_\theta)^{\mathrm{T}} + (\boldsymbol{H}_u)\, \boldsymbol{\mu}^{\mathrm{T}} (\boldsymbol{B}_\theta)^{\mathrm{T}}] d\Omega_e \tag{39b}$$

$$\boldsymbol{A}_{\theta U} = \sum_e \int_{\Omega_e} [(\boldsymbol{B}_\theta)\boldsymbol{e}^{\mathrm{T}}(\boldsymbol{B}_u)^{\mathrm{T}} + (\boldsymbol{B}_\theta)\boldsymbol{\mu}\,(\boldsymbol{H}_u)^{\mathrm{T}}] d\Omega_e \tag{39c}$$

$$\boldsymbol{A}_{\theta\theta} = -\sum_e \int_{\Omega_e} (\boldsymbol{B}_\theta)\boldsymbol{\kappa}(\boldsymbol{B}_\theta)^{\mathrm{T}} d\Omega_e \tag{39d}$$

$$\boldsymbol{f}_U = \sum_e \int_{\Gamma_{te}} \boldsymbol{N}_u^T \boldsymbol{t}_\Gamma d\Gamma_{te} \tag{39e}$$

$$\boldsymbol{f}_\theta = -\sum_e \int_{\Gamma_{De}} \boldsymbol{N}_\theta^T \omega d\Gamma_{De}. \tag{39f}$$

In Eqs. (39a)–(39f), the subscript, e, in Ω_e, Γ_{te} and Γ_{De} denotes the eth finite element where $\Omega = \cup_e \Omega_e$. Moreover, $\boldsymbol{C}$, $\boldsymbol{\kappa}$, $\boldsymbol{e}$ and $\boldsymbol{\mu}$ can be written in matrix form as

$$\boldsymbol{C} = \left(\frac{Y}{(1+\nu)(1-2\nu)}\right) \begin{bmatrix} 1-\nu & \nu & 0 \\ \nu & 1-\nu & 0 \\ 0 & 0 & \left(\frac{1}{2}-\nu\right) \end{bmatrix} \tag{40a}$$

$$\boldsymbol{\kappa} = \begin{bmatrix} \kappa_{11} & 0 \\ 0 & \kappa_{33} \end{bmatrix} \tag{40b}$$

$$\boldsymbol{e}^T = \begin{bmatrix} 0 & 0 & e_{15} \\ e_{31} & e_{33} & 0 \end{bmatrix} \tag{40c}$$

$$\boldsymbol{\mu} = \begin{bmatrix} \mu_{11} & \mu_{12} & 0 & 0 & 0 & \mu_{44} \\ 0 & 0 & \mu_{44} & \mu_{12} & \mu_{11} & 0 \end{bmatrix}$$

where ν denotes Poisson's ratio and Y is the Young's modulus. (40d)

Interested readers can also refer to [1,10] for more details about the theory of flexoelectricity.

4. Level Set Method (LSM) and optimization problem

4.1. LSM

In this section we briefly describe the LSM fundamentals. We assume $\Omega \subset D_\Omega \subset \mathbb{R}^d$ ($d = 2$ or 3), where D_Ω is the whole structural domain including all admissible shapes, Ω. A level set function $\Phi(\boldsymbol{x})$ is defined as

$$\begin{array}{rll} \text{Solid}: & \Phi(\boldsymbol{x}) > 0 & \forall \boldsymbol{x} \in \Omega \setminus \partial\Omega \\ \text{Boundary}: & \Phi(\boldsymbol{x}) = 0 & \forall \boldsymbol{x} \in \partial\Omega \cap D_\Omega \\ \text{Void}: & \Phi(\boldsymbol{x}) < 0 & \forall \boldsymbol{x} \in D_\Omega \setminus \Omega. \end{array} \tag{41}$$

The design boundary $\Gamma(\boldsymbol{x})$ is then implicitly represented by the iso-surface (in this text zero surface) of $\Phi(\boldsymbol{x})$ such that

$$\Gamma(\boldsymbol{x}) = \left\{\boldsymbol{x} \in \mathbb{R}^d \,|\, \Phi(\boldsymbol{x}) = 0\right\} \tag{42}$$

and by letting the level set function dynamically change in time, the dynamic model is expressed as

$$\Gamma(t) = \left\{\boldsymbol{x}(t) \in \mathbb{R}^d \,|\, \Phi(\boldsymbol{x}(t), t) = 0\right\} \tag{43}$$

and by differentiating both sides of Eq. (43) with respect to time and applying the chain rule we have

$$\frac{\partial \Phi(\boldsymbol{x}(t), t)}{\partial t} + \nabla \Phi(\boldsymbol{x}(t), t) . \frac{d\boldsymbol{x}}{dt} = 0 \tag{44}$$

where $\boldsymbol{V} = \frac{d\boldsymbol{x}}{dt}$ is the velocity vector of the design boundary and its normal component is $V_n = \boldsymbol{V}.\boldsymbol{n}$ where $\boldsymbol{n} = \frac{\nabla \Phi}{|\nabla \Phi|}$ is the unit outward normal to the boundary. Eq. (44) is the so-called Hamilton–Jacobi equation and can be written in the form of

$$\frac{\partial \Phi}{\partial t} + V_n \left|\nabla \Phi\right| = 0 \tag{45}$$

which defines an initial value problem for the time dependent function Φ. In optimization process V_n is the movement of a point on a surface driven by the objective of the optimization. The optimal structural boundary is then expressed as a solution of Eq. (45) obtained by a so called "up-wind scheme" [20].

In this paper, the LS function at the point (x, y) is denoted by $\Phi(x, y)$ and defined as

$$\Phi(x, y) = \sum_{i=1}^{ncp} \sum_{j=1}^{mcp} N_{i,j}^{p,q}(\xi, \eta)\, \varphi_{i,j} \tag{46}$$

where $N_{i,j}^{p,q}$ and $\varphi_{i,j}$ are B-spline basis functions and corresponding nodal values of LS, respectively. $\varphi_{i,j}$ are the only design variables which are defined on the control points mesh being set as the signed distance to the given boundary of the initial design.

The density-based approach is used for mapping the geometry to the mechanical model. Using this approach, the material domain (density field $0 < \rho_{\min} \leq \rho(\boldsymbol{x}) \leq 1$) flows through a fixed discretization of the design domain in each optimization iteration. In other words, these densities are used to directly scale the stiffness of the material, known as the "Ersatz material" approach. $\rho = 1$ represents the solid material while $\rho_{\min} = 1e^{-4}$ is the lower bound to avoid singularity of the stiffness matrix.

Using point-wise mapping to control an element-wise constant density distribution we have

$$\rho_e = (1 - \rho_{\min})\, \widetilde{H}(\Phi(X_e)) + \rho_{\min} \tag{47}$$

where X_e is the center of a finite element e. $\widetilde{H}(\Phi)$ is a smooth approximation of the Heaviside function defined by [20]

$$\widetilde{H}(\Phi) = \begin{cases} 0 & \text{for } \Phi < -\Delta \\ -\frac{1}{4}\left(\frac{\Phi}{\Delta}\right)^3 + \frac{3}{4}\left(\frac{\Phi}{\Delta}\right) + \frac{1}{2} & \text{for } -\Delta \leq \Phi \leq \Delta \\ 1 & \text{for } \Delta < \Phi. \end{cases} \tag{48}$$

where Δ is the width of numerical approximation. Having ρ, the volume integrals of some functional f over a material domain can then be defined as

$$\int_{\Omega} f dV = \int_{D} f \widetilde{H}(\Phi) dV \approx \int_{D} f \rho(\Phi)\, dV. \tag{49}$$

Meanwhile ρ is embedded in the electromechanical problem as

$$\boldsymbol{M}(x, y) = \rho(\Phi)\ \boldsymbol{M}_0 \quad \text{with } \boldsymbol{M}_0 = \boldsymbol{C},\ \boldsymbol{e},\ \boldsymbol{\kappa},\ \boldsymbol{\mu} \tag{50}$$

where $\boldsymbol{C}$, $\boldsymbol{e}$, $\boldsymbol{\kappa}$ and $\boldsymbol{\mu}$ denote elastic, piezoelectricity, permittivity and flexoelectricity tensors, respectively. Subscript 0 represents properties of the solid material.

The derivative of the density function with respect to the level set nodal values is obtained by

$$\frac{\partial \rho_e}{\partial \varphi_{i,j}} = (1 - \rho_{\min}) \tilde{\delta}(\Phi(X_e)) \frac{\partial \Phi(X_e)}{\partial \varphi_{i,j}} \tag{51}$$

where $\tilde{\delta}(\Phi) = \frac{\partial \widetilde{H}}{\partial \Phi}$ is the approximate Dirac delta function defined by

$$\tilde{\delta}(\Phi) = \begin{cases} \frac{3(1 - \rho_{\min})}{4\Delta}\left(1 - \left(\frac{\Phi}{\Delta}\right)^2\right) & \text{for } -\Delta \leq \Phi \leq \Delta \\ 0 & \text{otherwise} \end{cases} \tag{52}$$

and $\frac{\partial \Phi(X_e)}{\partial \varphi_{i,j}}$ is calculated by

$$\frac{\partial \Phi(X_e)}{\partial \varphi_{i,j}} = R_{i,j}^{p,q}(\xi, \eta). \tag{53}$$

4.2. Optimization problem

The electromechanical coupling coefficient, k_{eff}^2, is defined as

$$k_{eff}^2 = \frac{w_{elec}}{w_{mech}} \tag{54}$$

where w_{elec} and w_{mech} are the electrical and mechanical (or strain) energies, respectively. By extending w_{elec} and w_{mech} in Eq. (54) and defining the objective function, $J(\boldsymbol{u}(\boldsymbol{\varphi}), \boldsymbol{\theta}(\boldsymbol{\varphi}), \boldsymbol{\varphi})$, as the inverse of k_{eff}^2 we have

$$J(\boldsymbol{u}(\boldsymbol{\varphi}), \boldsymbol{\theta}(\boldsymbol{\varphi}), \boldsymbol{\varphi}) = \frac{1}{k_{eff}^2} = \frac{w_{mech}}{w_{elec}} = \frac{\frac{1}{2}\int_\Omega \boldsymbol{\varepsilon}^{\mathrm{T}} \boldsymbol{C} \boldsymbol{\varepsilon}\, d\Omega}{\frac{1}{2}\int_\Omega \boldsymbol{E}^{\mathrm{T}} \boldsymbol{\kappa} \boldsymbol{E}\, d\Omega} \tag{55}$$

where $\boldsymbol{\varepsilon}$ and $\boldsymbol{E}$ are obtained according to Eqs. (36c)–(36d) and $\boldsymbol{\varphi}$ denotes the vector containing all $\varphi_{i,j}$. Eventually, the optimization problem can be summarized as follows

$$\begin{aligned} &\text{Minimize}: J(\boldsymbol{u}(\boldsymbol{\varphi}), \boldsymbol{\theta}(\boldsymbol{\varphi}), \boldsymbol{\varphi}) \\ &\text{Subjected to}: \\ &V_f = \int_D \rho(\Phi)\, dV \le V_{f0} \\ &\begin{bmatrix} \boldsymbol{A}_{UU} & \boldsymbol{A}_{U\theta} \\ \boldsymbol{A}_{\theta U} & \boldsymbol{A}_{\theta\theta} \end{bmatrix} \begin{bmatrix} \mathbf{U} \\ \theta \end{bmatrix} = \begin{bmatrix} \boldsymbol{f}_U \\ \boldsymbol{f}_\theta \end{bmatrix} \end{aligned} \tag{56}$$

where V_f is the total volume in each optimization iteration; V_{f0} is an arbitrary volume which must be set at the beginning of the optimization process. By introducing a proper Lagrangian objective function, l, and Lagrange multiplier, ψ, we obtain

$$l = J - \psi\left(V_f - V_{f0}\right). \tag{57}$$

To find the minimum of l, we set the first derivatives of Eq. (57) with respect to $\boldsymbol{\varphi}$ as zero. So,

$$\frac{dl}{d\boldsymbol{\varphi}} = \frac{dJ}{d\boldsymbol{\varphi}} - \psi \frac{dV_f}{d\boldsymbol{\varphi}} = 0. \tag{58}$$

To update the design variables, sensitivity analysis is required which is presented in Section 4.3.

4.3. Sensitivity analysis

To solve Eq. (58), one should differentiate the objective and constraint functions with respect to the design variables. Considering the coupled system of equations in residual form, we have

$$\boldsymbol{R}_1^*(\boldsymbol{u}, \boldsymbol{\theta}) = \mathbf{0} \tag{59a}$$

$$\boldsymbol{R}_2^*(\boldsymbol{u}, \boldsymbol{\theta}) = \mathbf{0} \tag{59b}$$

where $\boldsymbol{R}_1^*$ and $\boldsymbol{R}_2^*$ are residuals that must be simultaneously satisfied, and $\boldsymbol{u}$ and $\boldsymbol{\theta}$ are solution (i.e. displacement and electric potential) fields. By assembling Eqs. (59a) and (59b) into a single global residual $\mathfrak{R}$ we have

$$\mathfrak{R}(\mathfrak{U}) = \begin{bmatrix} \boldsymbol{R}_1^*(\boldsymbol{u}, \boldsymbol{\theta}) \\ \boldsymbol{R}_2^*(\boldsymbol{u}, \boldsymbol{\theta}) \end{bmatrix} = \mathfrak{R}(\mathfrak{U}(\boldsymbol{\varphi}), \boldsymbol{\varphi}) = \mathbf{0} \tag{60}$$

where

$$\mathfrak{U} = \begin{bmatrix} \boldsymbol{u} \\ \boldsymbol{\theta} \end{bmatrix}. \tag{61}$$

Thus, the objective function takes the form $J(\mathfrak{U}(\boldsymbol{\varphi}), \boldsymbol{\varphi})$. Recalling Eq. (58), we use the chain-rule to calculate the sensitivity of $J(\mathfrak{U}(\boldsymbol{\varphi}), \boldsymbol{\varphi})$ with respect to $\boldsymbol{\varphi}$. So,

$$\frac{dJ}{d\boldsymbol{\varphi}} = \frac{\partial J}{\partial \mathfrak{U}} \frac{\partial \mathfrak{U}}{\partial \boldsymbol{\varphi}} + \frac{\partial J}{\partial \boldsymbol{\varphi}}. \tag{62}$$

The last term of Eq. (62) is the explicit quantity and easy to calculate

$$\frac{\partial J}{\partial \boldsymbol{\varphi}} = \frac{1}{w_{elec}} \left(\frac{1}{2} \int_{\Omega} \boldsymbol{\varepsilon}^{\mathrm{T}} \frac{\partial \boldsymbol{C}}{\partial \boldsymbol{\varphi}} \boldsymbol{\varepsilon} \, d\Omega \right) - \frac{w_{mech}}{w_{elec}^2} \left(\frac{1}{2} \int_{\Omega} \boldsymbol{E}^{\mathrm{T}} \frac{\partial \boldsymbol{\kappa}}{\partial \boldsymbol{\varphi}} \boldsymbol{E} \, d\Omega \right) \tag{63}$$

while w_{elec} and w_{mech} are calculated according to Eq. (55); For plane strain problem

$$\frac{\partial \boldsymbol{C}}{\partial \boldsymbol{\varphi}} = \frac{\partial \rho_e}{\partial \boldsymbol{\varphi}} \left(\frac{Y}{(1+\nu)(1-2\nu)} \right) \begin{bmatrix} 1-\nu & \nu & 0 \\ \nu & 1-\nu & 0 \\ 0 & 0 & \left(\frac{1}{2} - \nu\right) \end{bmatrix} \tag{64}$$

and

$$\frac{\partial \boldsymbol{\kappa}}{\partial \boldsymbol{\varphi}} = \frac{\partial \rho_e}{\partial \boldsymbol{\varphi}} \begin{bmatrix} \kappa_{11} & 0 \\ 0 & \kappa_{33} \end{bmatrix} \tag{65}$$

where $\frac{\partial \rho_e}{\partial \boldsymbol{\varphi}}$ is obtained according to Eq. (51). To calculate $\frac{\partial \mathfrak{U}}{\partial \boldsymbol{\varphi}}$ as an implicit quantity, we differentiate Eq. (60) as

$$\left(\frac{\partial \mathfrak{R}}{\partial \mathfrak{U}} \right)^{\mathrm{T}} \frac{\partial \mathfrak{U}}{\partial \boldsymbol{\varphi}} + \frac{\partial \mathfrak{R}}{\partial \boldsymbol{\varphi}} = 0 \tag{66}$$

$$\frac{\partial \mathfrak{U}}{\partial \boldsymbol{\varphi}} = - \left(\frac{\partial \mathfrak{R}}{\partial \mathfrak{U}} \right)^{-\mathrm{T}} \frac{\partial \mathfrak{R}}{\partial \boldsymbol{\varphi}} \tag{67}$$

substituting Eq. (67) into the first term of Eq. (62) right hand side yields

$$\frac{\partial J}{\partial \mathfrak{U}} \frac{\partial \mathfrak{U}}{\partial \boldsymbol{\varphi}} = - \frac{\partial J}{\partial \mathfrak{U}} \left[\left(\frac{\partial \mathfrak{R}}{\partial \mathfrak{U}} \right)^{-\mathrm{T}} \frac{\partial \mathfrak{R}}{\partial \boldsymbol{\varphi}} \right] \tag{68}$$

assuming

$$\boldsymbol{\lambda} = - \frac{\partial J}{\partial \mathfrak{U}} \left(\frac{\partial \mathfrak{R}}{\partial \mathfrak{U}} \right)^{-\mathrm{T}} \tag{69}$$

and knowing that $\frac{\partial \mathfrak{R}}{\partial \mathfrak{U}} = \boldsymbol{K}_{\text{total}}$, we can write

$$\boldsymbol{K}_{\text{total}} \boldsymbol{\lambda} = - \frac{\partial J}{\partial \mathfrak{U}} \tag{70}$$

$$\boldsymbol{K}_{\text{total}} \boldsymbol{\lambda} = - \frac{1}{w_{elec}} \int_{\Omega} \boldsymbol{B}_u \boldsymbol{C} (\boldsymbol{B}_u)^{\mathrm{T}} \boldsymbol{u} \, d\Omega + \frac{w_{mech}}{w_{elec}^2} \int_{\Omega} \boldsymbol{B}_\theta \boldsymbol{\kappa} (\boldsymbol{B}_\theta)^{\mathrm{T}} \boldsymbol{\theta} \, d\Omega \tag{71}$$

eventually, Eq. (68) can be written in the form

$$\frac{\partial J}{\partial \mathfrak{U}} \frac{\partial \mathfrak{U}}{\partial \boldsymbol{\varphi}} = (\boldsymbol{\lambda})^{\mathrm{T}} \frac{\partial \mathfrak{R}}{\partial \boldsymbol{\varphi}} \tag{72}$$

Table 1
The cantilever beam problem: material properties, geometry and load data.

L/h	υ	Y	e_{31}	μ_{12}	κ_{11}	κ_{33}	χ_{33}	F
20	0.37	100 GPa	-4.4 C/m^2	1 μC/m	11 nC/Vm	12.48 nC/Vm	1408	100 μN

$\frac{L}{h}$: beam aspect ratio, ν : Poisson ratio, Y : Young's modulus, e_{31} : piezoelectric constant.
μ_{12} : flexoelectric constant, κ_{11} and κ_{33} : dielectric constants, χ_{33} : electric susceptibility, F : point load.

$$\frac{\partial J}{\partial \mathfrak{U}}\frac{\partial \mathfrak{U}}{\partial \boldsymbol{\varphi}} = \begin{bmatrix} A'_{UU} & A'_{U\theta} \\ A'_{\theta U} & A'_{\theta\theta} \end{bmatrix} [\boldsymbol{\lambda}] \tag{73}$$

$$A'_{UU} = \int_{\Omega} \boldsymbol{u}^{\mathrm{T}} \left(\boldsymbol{B}_u \frac{\partial C}{\partial \boldsymbol{\varphi}} \boldsymbol{B}_u^{\mathrm{T}} \right) d\Omega \tag{74}$$

$$A'_{U\theta} = \int_{\Omega} \boldsymbol{u}^{\mathrm{T}} \left(\boldsymbol{B}_u \frac{\partial \boldsymbol{e}}{\partial \boldsymbol{\varphi}} \boldsymbol{B}_\theta^{\mathrm{T}} + \boldsymbol{H}_u \frac{\partial \boldsymbol{\mu}}{\partial \boldsymbol{\varphi}}^{\mathrm{T}} \boldsymbol{B}_\theta^{\mathrm{T}} \right) d\Omega \tag{75}$$

$$A'_{\theta U} = \int_{\Omega} \boldsymbol{\theta}^{\mathrm{T}} \left(\boldsymbol{B}_\theta \frac{\partial \boldsymbol{e}}{\partial \boldsymbol{\varphi}}^{\mathrm{T}} \boldsymbol{B}_u^{\mathrm{T}} + \boldsymbol{B}_\theta \frac{\partial \boldsymbol{\mu}}{\partial \boldsymbol{\varphi}} \boldsymbol{H}_u^{\mathrm{T}} \right) d\Omega \tag{76}$$

$$A'_{\theta\theta} = -\int_{\Omega} \boldsymbol{\theta}^{\mathrm{T}} \left(\boldsymbol{B}_\theta \frac{\partial \boldsymbol{\kappa}}{\partial \boldsymbol{\varphi}} \boldsymbol{B}_\theta^{\mathrm{T}} \right) d\Omega \tag{77}$$

where

$$\frac{\partial \boldsymbol{e}}{\partial \boldsymbol{\varphi}}^{\mathrm{T}} = \frac{\partial \rho_e}{\partial \boldsymbol{\varphi}} \begin{bmatrix} 0 & 0 & e_{15} \\ e_{31} & e_{33} & 0 \end{bmatrix} \tag{78}$$

and

$$\frac{\partial \boldsymbol{\mu}}{\partial \boldsymbol{\varphi}} = \frac{\partial \rho_e}{\partial \boldsymbol{\varphi}} \begin{bmatrix} \mu_{11} & \mu_{12} & 0 & 0 & 0 & \mu_{44} \\ 0 & 0 & \mu_{44} & \mu_{12} & \mu_{11} & 0 \end{bmatrix} \tag{79}$$

and finally, for the last term of Eq. (58) we have

$$\frac{dV_f}{d\boldsymbol{\varphi}} = \frac{\partial V_f}{\partial \boldsymbol{\varphi}} = \int_{\Omega} \frac{\partial \rho_e}{\partial \boldsymbol{\varphi}} d\Omega \tag{80}$$

which is already obtained according to Eq. (51).

5. Numerical examples

In this section, we first verify our analysis model by comparing our results with some benchmark examples. The verified IGA model is then employed in the optimization algorithm to demonstrate its validity and usefulness. We assume isotropic linear elasticity under plane strain conditions in all examples. Commonly studied flexoelectric configurations (cantilever beam and truncated pyramid) with different electrical boundary conditions are solved. Electrodes are assumed as very thin deposited layers on the structures to impose equipotential boundary conditions, and have no contribution to the structural stiffness.

5.1. Verification of the IGA model

5.1.1. Cantilever beam (mechanical loading)

Fig. 2(a) and (b) schematically represent the cantilever beam with mechanical and electrical boundary conditions. The model is discretized by 50×10 B-spline elements of order 3. The red dots represent the control points as shown in Fig. 2(c). Material properties of $BaTiO_3$ and loading data as listed in Table 1 are considered based on [12].

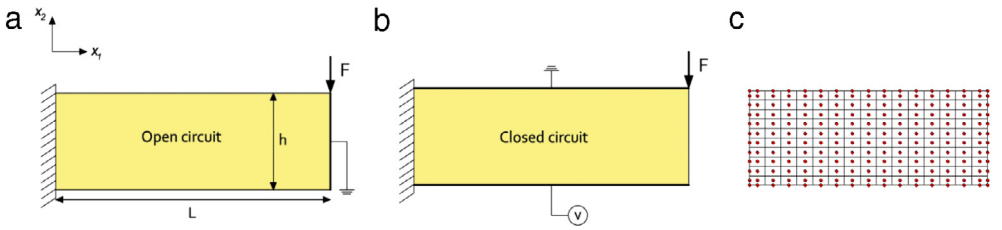

Fig. 2. Electromechanical boundary conditions for open circuit (a) and closed circuit (b), FE discretization with red dots representing the control points (c).

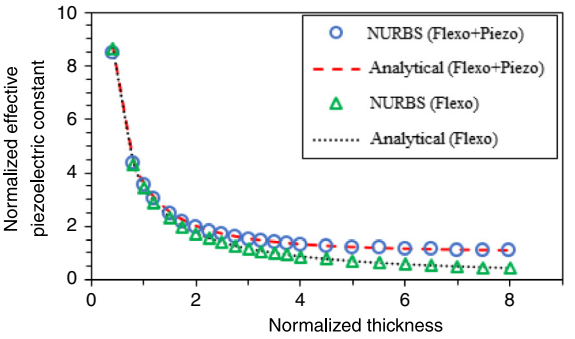

Fig. 3. Normalized effective piezoelectric constant e' versus normalized beam thickness h'. Graphs are for open circuit conditions and contain both piezoelectric and non-piezoelectric materials. The results for analytic solutions are reproduced according to Eq. (81).

Following the terminologies of our benchmark examples [12] and assuming that the only non-zero component of the stress is σ_{11} and of the electric field is E_2, for one-dimensional coupling, Eq. (54) is analytically estimated in [10] as

$$k_{eff} = \frac{\chi}{1+\chi}\sqrt{\frac{\kappa}{Y}\left(e^2 + 12\left(\frac{\mu}{h}\right)^2\right)} \tag{81}$$

where the normalized effective piezoelectric constant is

$$e' = \frac{k_{eff}}{k_{piezo}} \tag{82}$$

where k_{piezo} is obtained by neglecting flexoelectricity ($\mu = 0$) in Eq. (81).

To numerically simulate a 1-D coupling, we simplify our model by setting Poisson's ratio as well as all piezoelectric and flexoelectric constants to zero except e_{31} and μ_{12} which take the corresponding values of Table 1. Fig. 3 compares the results of the present and the analytical methods for both piezoelectric and non-piezoelectric materials. Here h' is the normalized beam thickness and for the open circuit condition is obtained by $h' = -eh/\mu$. The non-piezoelectric materials are also obtained by setting $e_{31} = 0$. Fig. 3 illustrates that when the thickness of the beam decreases, the electromechanical response of the beam increases. This enhancement in electromechanical response at small length scales has also been observed for non-piezoelectric materials. Furthermore, as expected the flexoelectric effect vanishes for larger beam thicknesses. Overall, we observe excellent agreement between the results of the current method and the analytical solutions.

5.1.2. Cantilever beam (electrical loading)

For our next example we study a cantilever beam acting as an electromechanical actuator. The beam is 50 μm long, 2.5 μm high, is made of non-piezoelectric material and has the closed circuit configuration as illustrated in Fig. 2. A voltage V equal to -20 MV is applied to the bottom edge while the top edge is grounded. The mechanical point load, F, is also set to zero.

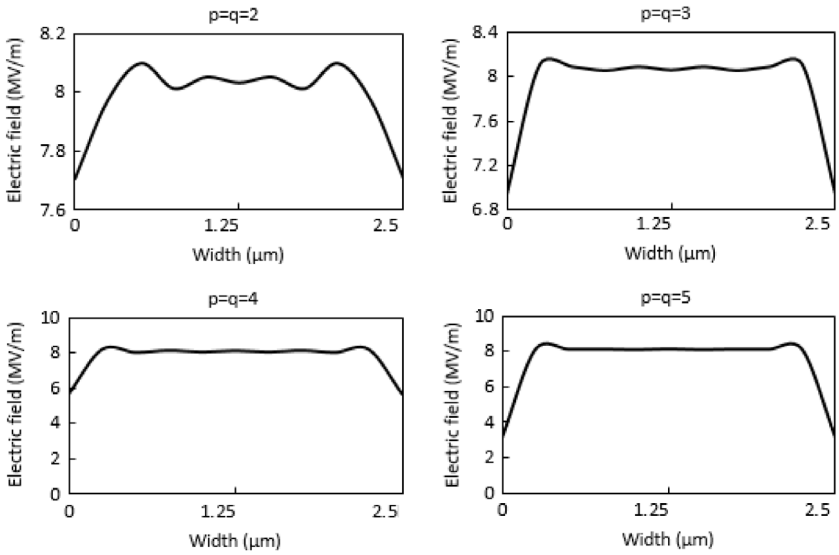

Fig. 4. Distribution of electric field across the beam thickness for different orders of basis functions. p and q are order of basis functions in direction of length and width of the beam, respectively.

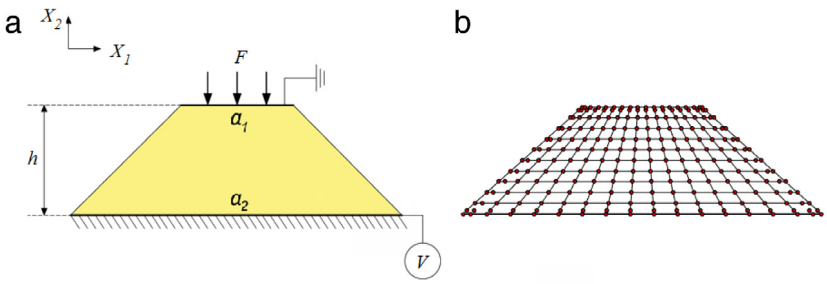

Fig. 5. Truncated pyramid under compression, problem setup (a), FE discretization (b).

For above settings, the only phenomenon that deforms the beam is flexoelectricity, which acts as a result of polarization gradients. To demonstrate this, the distribution of the electric field across the beam thickness at the mid length of the beam is graphed in Fig. 4. The results are slightly dependent on the order of the basis functions. In particular, larger gradients near the surfaces are obtained with increasing basis functions order. Our results, which are converged on a sufficiently fine discretization, are in good agreement with the benchmark example [12] from both values and field distribution points of view. All graphs clearly represent the high gradients at the top and bottom surfaces of the beam, which generate mechanical stresses and eventually deform the beam. The electric field is represented more smoothly away from the surfaces using higher orders basis functions.

5.1.3. Truncated pyramid

For the next example we investigate the flexoelectric effect in a truncated pyramid under compression; this geometry has been widely studied in flexoelectricity [24] because of the intrinsic generation of strain gradients due to the different widths of the top and bottom surfaces. A uniformly distributed force of magnitude F is applied on the top edge while the bottom edge is mechanically fixed. The problem configuration and its FE discretization are shown in Fig. 5. The material parameters are according to Table 1 while the other design parameters are listed in Table 2.

Fig. 6 shows the distribution of the electric potential (left) and the resulted strain in Y direction, ε_{22}, (right). Once again there is an acceptable agreement, in both patterns and values, between the results of the present method and [12].

Table 2
The truncated pyramid problem: geometry and load data.

a_1	a_2	h	F
750 μm	2250 μm	750 μm	6 $\frac{\text{N}}{\mu\text{m}}$

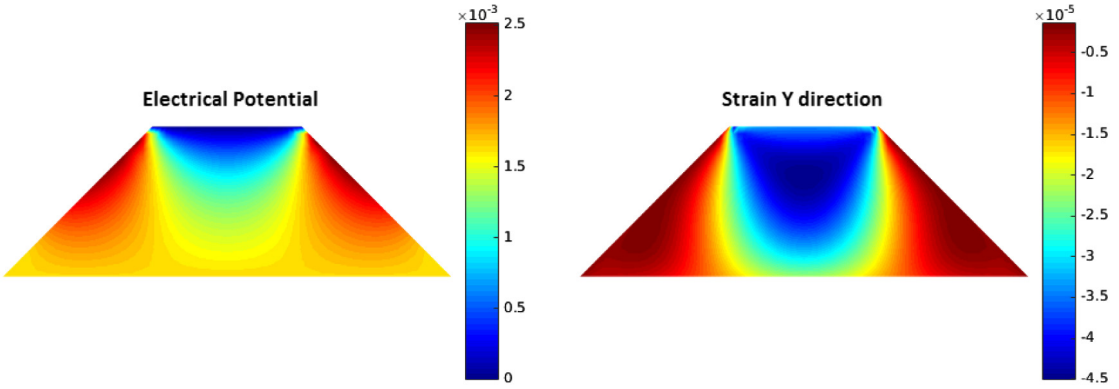

Fig. 6. Distribution of the electric potential **(left)** and strain in Y direction, ε_{22} **(right)**.

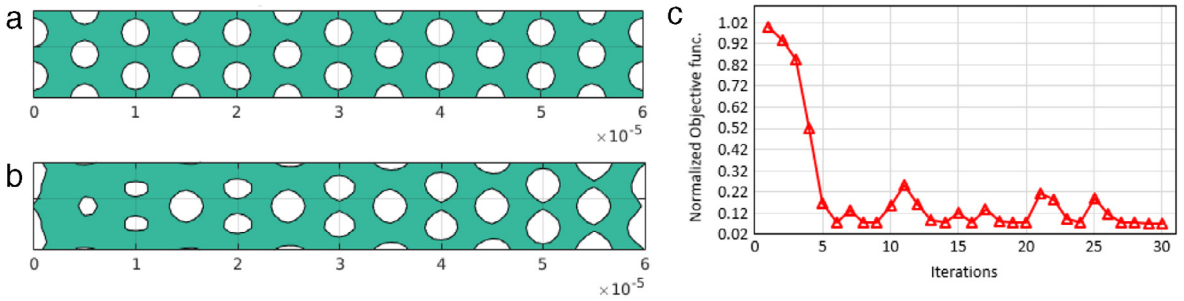

Fig. 7. Initial (a) and the optimized (b) topologies considering 70% of the solid beam volume as design constraint. Normalized objective function versus iterations is plotted in (c). The beam is made of non-piezoelectric material with open circuit boundary conditions. The length of the beam is 60 μm with aspect ratio of 7.

5.2. *Topology optimization of the flexoelectric beam*

Since there is no benchmark topology optimization example available for flexoelectricity, we have initially verified our methodology for an elastic (by setting all the electrical parameters to zero) cantilever beam subjected to a mechanical load [25].

We now consider a cantilever beam of length 60 μm with an aspect ratio (defined by the beam length over its height) of 7. It is made of non-piezoelectric material ($e_{31} = 0$) with open circuit boundary conditions. The loading and other material constants are according to Table 1. The objective function in all the following examples is minimizing the inverse of k^2_{eff}, as defined by Eq. (55). Fig. 7(a)–(c) show the initial Fig. 7(a) and the optimized Fig. 7(b) topologies constrained by 70% of the solid beam volume as the design limit.

To understand the optimum topology seen in Fig. 7(b), we emphasize that for flexoelectric materials, electric polarization displays a linear relationship to the gradient of mechanical strain (see Eq. (2)) while for piezoelectric materials, the electric polarization and the mechanical strain are interrelated (see Eq. (1)). Thus, for flexoelectric structures, recognizing the zones with high strain gradients in the structure is the key to interpret the optimal topology. In Fig. 7(b) it is observed that more material is available in the left half (including fixed edge) of the structure (where the strain and strain gradients are higher) rather than the right half (including free edge). Within the left half, the material is also more available on top and bottom edges rather than the central part of the beam, for the same reason. The shape of the fixed edge is also in line with more electrical energy generation, as our detailed investigations

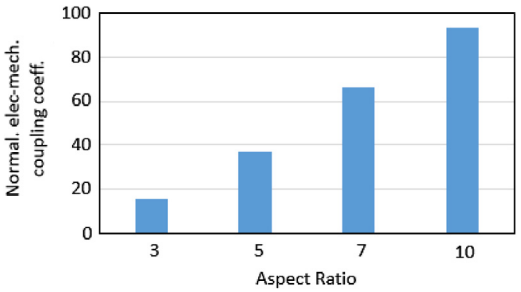

Fig. 8. k_{eff}^{N} versus beam aspect ratio. k_{eff}^{N} is the ratio of the electromechanical coupling coefficients of the optimized structure to the solid structure. For all cases, the length of the beam is 60 μm and the optimized topology has 70% of the solid beam volume.

have shown that material reduction along the fixed edge will increase the generated electrical energy. Thus overall, the optimized geometry is in line with maximizing the electromechanical coupling coefficient which is equivalent to minimizing the objective function. The history of the objective function, which converges towards the minimum value, is presented in (7(c)).

We define k_{eff}^{sld} and k_{eff}^{opt} as parameters that define the electromechanical coupling coefficients of the solid and optimized structures, respectively. In this case $k_{eff}^{sld} = 4.75e^{-5}$ and $k_{eff}^{opt} = 315e^{-5}$ and their ratio, $k_{eff}^{N} = \frac{k_{eff}^{opt}}{k_{eff}^{sld}} = 66.32$, is the normalized electromechanical coupling coefficient. That would be a reasonable argument that such an increase in energy conversion is partially due to 30% decrease in structural volume; we declare that the electromechanical coupling coefficient for the initial structure (Fig. 7(a)), k_{eff}^{ini}, which has nearly the same volume as the optimized structure (i.e. 70% of the solid beam volume), is equal to $22.5e^{-5}$. By comparison of these numbers ($\frac{k_{eff}^{opt}}{k_{eff}^{ini}} = 14$) we can determine how significant the role of topology optimization in increasing k_{eff} is. We performed similar analysis for different beam aspect ratios, plotted in Fig. 8. It is observable that, the higher the aspect ratio, the higher k_{eff}^{N} is obtained. It means topology optimization shows profound advantages in higher aspect ratios.

We now consider the flexoelectric truncated pyramid under a 10 μN point load applied at the midpoint of the top edge. Other design parameters and dimensions are listed in Tables 1 and 2 considering 70% of the solid truncated pyramid volume as design constraint. Boundary conditions are according to Fig. 5. The optimized topology is shown in (Fig. 9(a)). The region with high strain gradients is located underneath the point load where the crown shape topology increases the strain gradients and consequently, the generated electrical energy. It is also observable that the length of the top edge has shortened, which also causes larger strain gradients.

The graph related to the history of the normalized objective function (Fig. 9(b)) and the graph for structural volume (Fig. 9(c)) converge relatively smoothly. The small jumps in graph of Fig. 9(b) at iterations 10, 20, 30 and 40 are related to re-initialization in optimization process. For this example $\frac{k_{eff}^{opt}}{k_{eff}^{ini}} = 2.47$ which shows again the impact of topology optimization on enhancing electromechanical behavior of dielectric solids possessing flexoelectric effect.

6. Concluding remarks

We have presented a computational framework for topology optimization of flexoelectric micro and nanostructures to enhance their energy conversion efficiency. Our methodology is based on a combination of isogeometric analysis (IGA), level set and point wise density mapping techniques. The smoothness of the IGA basis functions is used to discretize the fourth order partial differential equations of flexoelectricity, while the level set provides clear boundaries and gives stable convergence. The point wise density mapping is directly used in the weak form of the governing equations and its derivative can be consistently derived. The nodal level set values on control points and the inverse of the electromechanical coupling coefficient are defined as design variables and objective function, respectively. The numerical results demonstrate that B-spline elements can successfully model the flexoelectric effect in dielectrics. For a cantilever beam with constant length, it is shown that when the thickness of the beam decreases, the electromechanical response increases. The topology optimization is also able to noticeably increase

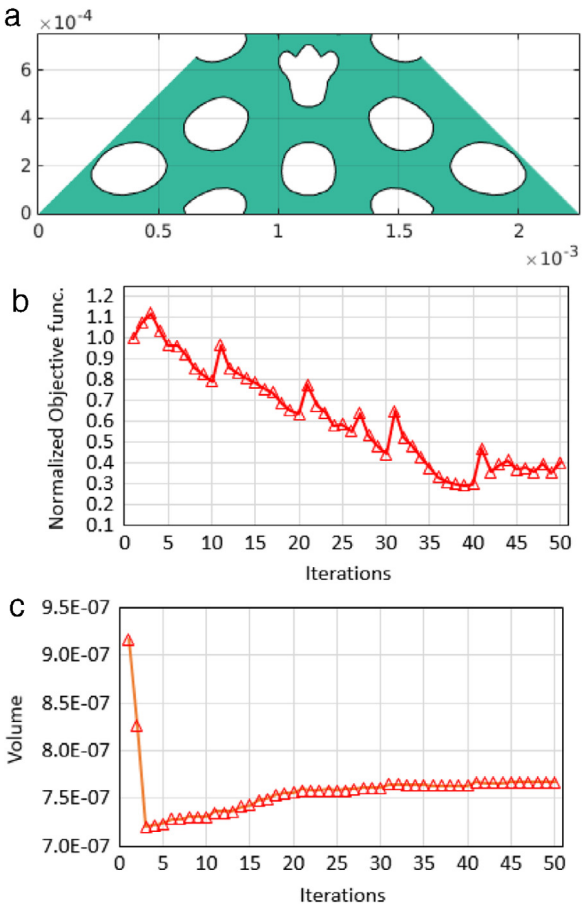

Fig. 9. The optimized topology (a) considering 70% of the solid truncated pyramid volume as design constraint. The normalized objective function versus iterations is plotted in (b) and the volume history is shown in (c). The pyramid is made of non-piezoelectric material under a 10 μN point load at mid of the top edge. The other design parameters are listed in Tables 1 and 2. The boundary conditions are shown in Fig. 5.

the electromechanical coupling coefficient, with substantial enhancements observed for higher aspect ratios. Overall, the presented computational methodology should contribute towards the design of micro and nano-scale flexoelectric devices with optimized electromechanical conversion efficiency.

Acknowledgments

The first author gratefully acknowledges the financial support of Ernst Abbe foundation within Nachwuchsförderprogramm. Harold Park acknowledges the support of the Mechanical Engineering Department at Boston University.

References

[1] N.D. Sharma, R. Maranganti, P. Sharma, On the possibility of piezoelectric nanocomposites without using piezoelectric materials, J. Mech. Phys. Solids 55 (2007) 2328–2350.
[2] S. Nanthakumar, T. Lahmer, X. Zhuang, G. Zi, T. Rabczuk, Detection of material interfaces using a regularized level set method in piezoelectric structures, Inverse Probl. Sci. Eng. 24 (1) (2016) 153–176.
[3] S.S. Nanthakumar, T. Lahmer, T. Rabczuk, Detection of multiple flaws in piezoelectric structures using XFEM and level sets, Comput. Methods Appl. Mech. Engrg. 275 (2014) 98–112.
[4] S.S. Nanthakumar, T. Lahmer, T. Rabczuk, Detection of flaws in piezoelectric structures using XFEM, Internat. J. Numer. Methods Engrg. 96 (6) (2013) 373–389.
[5] P.V. Yudin, A.K. Tagantsev, Topical review: Fundamentals of flexoelectricity in solids, Nanotechnology 24 (2013) 432001. http://dx.doi.org/10.1088/0957-4484/24/43/432001. 36pp.

[6] V.S. Mashkevich, K.B. Tolpygo, Electrical, optical and elastic properties of diamond crystals, Sov. Phys. JETP-USSR 5 (3) (1957) 435–439.
[7] F. Ahmadpour, P. Sharma, Flexoelectricity in two-dimensional crystalline and biological membranes, Nanoscale 7 (2015) 16555–16570.
[8] T.D. Nguyen, S. Mao, Y.-W. Yeh, P.K. Purohit, M.C. McAlpine, Nanoscale flexoelectricity, Adv. Mater. 25 (2013) 946–974.
[9] P. Zubko, G. Catalan, A.K. Tagantsev, Flexoelectric effect in solids, Annu. Rev. Mater. Res. 43 (2013) 387–421.
[10] M.S. Majdoub, P. Sharma, T. Cagin, Enhanced size-dependent piezoelectricity and elasticity in nanostructures due to the flexoelectric effect, Phys. Rev. B 79 (2009) 119904 (E).
[11] N.D. Sharma, C.M. Landis, P. Sharma, Piezoelectric thin-film super-lattices without using piezoelectric materials, J. Appl. Phys. 108 (2010) 024304.
[12] Amir Abdollahi, Christian Peco, Daniel Millan, Marino Arroyo, Irene Arias, Computational evaluation of the flexoelectric effect in dielectric solids, J. Appl. Phys. 116 (2014) 093502.
[13] Amir Abdollahi, Daniel Millan, Christian Peco, Marino Arroyo, Irene Arias, Revisiting pyramid compression to quantify flexoelectricity: A three-dimensional simulation study, Phys. Rev. B 91 (2015) 104103.
[14] M.P. Bendsøe, N. Kikuchi, Generating optimal topologies in structural design using a homogenization method, Comput. Methods Appl. Mech. Engrg. 71 (2) (1988) 197–224.
[15] Ole Sigmund, A 99 line topology optimization code written in Matlab, Struct. Multidiscip. Optim. 21 (2) (2001) 120–127.
[16] Ole Sigmund, On the design of compliant mechanisms using topology optimization, Mech. Struct. & Mach. 25 (4) (1997) 493–524.
[17] Ole Sigmund, Design of multiphysics actuators using topology optimization –Part I: One material structures, Comput. Methods Appl. Mech. Engrg. 190 (2001) 6577–6604.
[18] S.S. Nanthakumar, N. Valizadeh, Harold S. Park, Timon Rabczuk, Surface effects on shape and topology optimization of nanostructures, Comput. Mech. 56 (2015) 97–112.
[19] G.I.N. Rozvany, M. Zhou, T. Birker, Generalized shape optimization without homogenization, Struct. Multidiscip. Optim. 4 (1992) 250–254.
[20] Michael Yu Wang, Xiaoming Wang, Dongming Guo, A level set method for structural topology optimization, Comput. Methods Appl. Mech. Engrg. 192 (2003) 227–246.
[21] S. Osher, J.A. Sethian, Front propagating with curvature dependent speed: algorithms based on Hamilton-jacobi formulations, J. Comput. Phys. 78 (1988) 12–49.
[22] T.J.R. Hughes, J.A. Cottrell, Y. Bazilevs, Isogeometric analysis: CAD, finite elements, NURBS, exact geometry and mesh refinement, Comput. Methods Appl. Mech. Engrg. 194 (2005) 4135–4195.
[23] J.A. Cottrell, T.J.R. Hughes, Y. Bazilevs, Isogeometric Analysis Towards Integration of CAD and FEA, Wiley, UK, 2009.
[24] W.Y. Zhu, J.Y. Fu, N. Li, L. Cross, Piezoelectric composite based on the enhanced flexoelectric effects, Appl. Phys. Lett. 89 (2006) 192904.
[25] S. Shojaee, M. Mohamadian, N. Valizadeh, Composition of isogeometric analysis with level set method for structural topology optimization, Int. J. Optim. Civil Eng. 2 (1) (2012) 47–70.